Applications in Energy and Combustion Science 27 (2026) 100529

Contents lists available at ScienceDirect

Applications in Energy and Combustion Science

journal homepage: www.elsevier.com/locate/jaecs

Experimental characterization of a fuel-flexible burner with an integrated ultrasonic atomizer for low-carbon operation

Kristen Morse [a,*], Nele Kretzer [b], Chandra P. Singh [c], Jiawei Wan [c], Daniel Kretzler [d], Tobias Grimm [b], Björn Stelzner [d], Dimosthenis Trimis [d], Eva Gutheil [c], Jan T. Sehrt [b], Günter Brenn [a]

[a] Graz University of Technology, Institute of Fluid Mechanics and Heat Transfer (ISW), Graz, 8010, Austria
[b] Ruhr University Bochum, Chair of Hybrid Additive Manufacturing (HAM), Bochum, 44801, Germany
[c] Heidelberg University, Interdisciplinary Center for Scientific Computing (IWR) and Heidelberg Center for the Environment (HCE), Heidelberg, 69120, Germany
[d] Karlsruhe Institute of Technology, Engler-Bunte-Institute (EBI), Karlsruhe, 76131, Germany

ARTICLE INFO

Keywords:
Low-carbon
Fuel-flexible
Ammonia
Hydrogen
Alcohol
Additive manufacturing

ABSTRACT

The transition toward carbon-free combustion fuels such as hydrogen (H_2) and ammonia (NH_3) presents significant challenges related to flame stability and pollutant formation. Many carbon-free and low-carbon, fuel-flexible burners operate with either a gaseous or liquid-phase fuel, selecting only a single phase during stable operation. In this work, the newly developed HyMAm-Flex (v18) burner is experimentally characterized for multiphase, multi-fuel combustion at 18 distinct operating conditions, demonstrating stable flames of gaseous H_2, liquid ethanol (C_2H_5OH), and their binary and ternary mixtures with gaseous NH_3 under stoichiometric conditions. A key feature of the additively-manufactured burner is the integration of an ultrasonic atomizer, which enables the generation of sprays with a narrow size distribution and low injection velocities. The atomizer performance is evaluated in situ, demonstrating the stable operation in a combustion experiment. The primary objective of the present study is to provide an initial experimental characterization of the HyMAm-Flex (v18) burner concept and its fuel flexibility. Chemiluminescence measurements in combination with visible flame luminosity are used to qualitatively assess reaction-zone structure and discuss the flame stability. Exhaust gas measurements of ternary-fuel combinations provide a quantitative baseline of the burner's nitrogen-containing emissions and insight into the completeness of the combustion. Exhaust gas measurements showed nitrogen oxide (NO_x) < 400 ppmv (wet), NH_3 slip < 17 ppmv (wet), and nitrous oxide (N_2O) < 32 ppmv (dry). The addition of NH_3 is associated with reduced intensity in the central flame and increased N_2O and ammonia slip, whereas alcohol addition is associated with enhanced NH_3 combustion within an optimal blending range. This study demonstrates the fuel flexibility of the novel burner concept and discusses potential improvements to the burner design aimed at enhancing flame stability and overall performance.

1. Introduction

The urgent challenge of global warming has placed carbon dioxide emission reduction at the forefront of energy and combustion research [1,2]. The interest has shifted largely to transitioning burners toward the combustion of carbon-free fuels such as ammonia (NH_3) and hydrogen (H_2). However, these fuels introduce their own set of complexities and require careful design in order to limit pollutants [3].

Carbon-based fuels such as hydrocarbons and alcohols, including methane (CH_4), ethanol (C_2H_5OH), and methanol (CH_3OH), have characteristics that have made them ideal fuels for over a century, such as their favorable volumetric and gravimetric energy density [3,4]. These fuels are easy to ignite and maintain a controlled flame. In addition, carbon-based fuels are both easy to handle and well-proven in handling compared to alternative carbon-free fuels [4]. Despite their widespread use and favorable properties, the main product of combustion is the greenhouse gas carbon dioxide, CO_2. Advances in carbon-based fuel research have demonstrated the ability to synthesize C_2H_5OH and CH_3OH from biomass instead of the fossil sources, these are commonly referred to as "biofuels" [5]. In addition, scientists have also identified methods to produce CH_3OH in a carbon-neutral manner by using captured CO_2 and renewable H_2O [6].

* Corresponding author.
E-mail address: kristen.morse@tugraz.at (K. Morse).

https://doi.org/10.1016/j.jaecs.2026.100529
Received 26 March 2026; Received in revised form 15 June 2026; Accepted 16 June 2026
Available online 22 June 2026

The carbon-free fuel H_2 is both a very versatile and combustible fuel which makes it an excellent choice for the next-generation burners [7]. Hydrogen is an extremely reactive fuel: pure H_2 has a laminar flame speed that is five-fold faster than CH_3OH [4]. This high reactivity of premixed H_2 flames makes stable operation over a broad range of conditions challenging. Burner designs must prevent flashback at high H_2 concentrations while maintaining resistance to blow-off as the H_2 concentration decreases. The adiabatic flame temperature of stoichiometric premixed H_2–air flames at atmospheric conditions is approximately 300 K higher than that of CH_3OH–air flames [8]. Due to this elevated flame temperature, thermal NO_x formation is significantly enhanced in H_2–air combustion [8]. One method that has been explored to produce a stable hydrogen flame and limit NO_x formation is using the micro-combustion concept, proposed by Funke et al. [9], where the flow of H_2 is distributed to several sites to create small H_2 flamelets. Compared to a conventional flame, the micro-combustion concept produces smaller temperature gradients and much shorter residence times for the gases, which limits NO_x formation while maintaining stable combustion.

Ammonia is low in both gravimetric and volumetric energy density at ambient conditions; however, each NH_3 molecule contains three hydrogen atoms, giving it a higher volumetric hydrogen energy density than H_2 [10]. Pure NH_3 has a low flame temperature, low flame speed, and a low reactivity compared to conventional fuels [10]. As a result, NH_3 is often blended with carbon-based fuels or hydrogen to enhance its reactivity. Alternatively, it can be preheated to increase flame temperature and flame stability [11]. Ammonia combustion, especially when preheated, leads to the formation of the polluting combustion NO_x byproducts. Ammonia combustion can also produce the potent greenhouse gas N_2O. An additional challenge associated with NH_3 combustion is its extreme toxicity, which makes it difficult to handle [11].

As described above, each fuel has its own set of drawbacks and benefits. A burner that enables the flexible use of both carbon-neutral and carbon-free fuels can facilitate progress in understanding combustion mechanisms and identifying conditions under which the strengths of different fuels outweigh the limitations of any single fuel. Pitsch [7] highlights the need to develop new combustion devices that are fuel flexible. Pitsch argues that at this moment fuel flexibility, rather than relying solely on renewable fuels, is advantageous because renewable fuels are not currently available in sufficient quantities.

While many burners are designed for completely carbon-free combustion, focusing on stabilizing H_2 or NH_3–H_2 blend flames [12,13], numerous groups continue to consider carbon-based fuels as a means of enhancing flame stability [11,14–20]. Many of these groups study gaseous blends of carbon-based and carbon-free fuels. Compared to liquid fuels, such gaseous mixtures typically exhibit lower volumetric energy densities. This can impose constraints on burner design when attempting to stabilize NH_3-containing blends, which already suffer from an inherently low laminar flame speed.

To illustrate current approaches in low-carbon combustion, a few representative burners are highlighted. At Cardiff University [11,14–17], a fuel-flexible NH_3–H_2 and NH_3–CH_4 swirl burner for gas turbines was designed and experimentally characterized for a range of NH_3 blends [11,14–17]. In NH_3–H_2 testing, fuel blends from 50 vol% NH_3–50 vol% H_2 up to 90 vol% NH_3–10 vol% H_2 were operated in the generic swirl burner showing stable flame propagation was maintained, with H_2 addition significantly enhancing stability [14,15]. In this burner, stable combustion was achieved for lean mixtures, although higher NO_x emissions were observed for 50 vol% NH_3–50 vol% H_2 blends [16]. In NH_3–CH_4 and NH_3–H_2–CH_4 ternary studies, H_2 addition up to 30 vol% improved operability and reduced flame blow-off tendencies [16,17]. All NH_3–H_2–CH_4 blends tested reported NO_x emissions below 1000 ppmv (dry, normalized to 15% O_2), with lower NH_3 fractions producing higher NO_x and lower N_2O emissions [17].

A low-emission, fuel-flexible turbulent Bunsen burner was developed by Marshall et al. [18],Rajagopalan et al. [19], which operates with blends of H_2 and natural gas. Rajagopalan et al. [19] found that, in high H_2 fuel blends, increasing turbulence intensity and H_2 content both contributed to reduced CO levels due to enhanced oxidation and the lower carbon content of the fuel, while NO_x emissions were relatively invariant. The KAUST Double Swirl Burner (KDSB) is a co-combustion burner with a central NH_3 flame surrounded by an outer annular carbon-based flame [21]. Elbaz et al. [21] studied NH_3–natural gas flames in the KDSB to investigate flame structure and NO_x emissions. Building on this, Xu et al. [22] demonstrated that a methane outer flame can stabilize the NH_3 flame and significantly reduce NO emissions.

Fewer groups have studied burners that introduce multiphase mixtures of fuels. One such study is by Meng et al. [20] who investigated the impact of introducing CH_3OH for NH_3 cracking. Despite the many differences in approaches, the overarching goal remains the same: to minimize pollutant formation and reduce greenhouse gas emissions.

In the development of next-generation, fuel-flexible burners, new and developing technologies offer new opportunities for innovation. For instance, additive manufacturing (AM) has enabled the realization of complex burner geometries that were previously impractical or impossible to manufacture using traditional fabrication processes. This is true for porous media burners [23], micro-combustion burners [9], and swirl burners [24]. Another such technology, ultrasonic atomization, has seen limited application in combustion research [25,26]. However, this atomization approach offers distinct advantages for fuel-flexible systems, as it can generate fine sprays with a narrow size distribution and low injection velocities for a wide range of fuels [27].

Low droplet injection velocities increase the residence time of the droplets in the reaction zone. Additionally, in some situations the low velocities may enhance the flame stability by reducing the momentum of the fuel injection and allowing for a continuous, non-lifted flame structure [28]. In addition, a narrow size distribution, such as that produced by ultrasonic atomization [27], creates a more homogeneous mixture of fuels within the reaction zone.

This study investigates the HyMAm-Flex (v18) burner [29], a novel, fuel-flexible research burner that stabilizes NH_3 combustion with both a carbon-neutral and a carbon-free fuel. In this burner, the carbon-neutral liquid fuel is atomized with an ultrasonic atomizer, whose performance for combustion is also studied. The roles of additive manufacturing and numerical simulations in developing the burner architecture are discussed. This experimental campaign establishes a baseline of the burner's performance. In the experiments, fuel ratios are systematically varied to demonstrate the fuel flexibility of the burner. The baseline performance is characterized through chemiluminescence diagnostics, exhaust gas measurements, and visible flame luminosity.

2. Methods

This section overviews the design of the HyMAm-Flex burner, its fabrication and numerical investigation, and the experimental setup used for the combustion measurements.

2.1. Burner design

In this work, the HyMAm-Flex (v18), a novel, fuel-flexible research burner (< 10 kW) shown in Fig. 1 is studied, which was developed toward a more climate-friendly combustion process [29] and is fabricated using AM.

As described by Kretzer et al. [29], the HyMAm-Flex burner operates with two distinct combustion modes. The first strategy is based on a H_2 micro-combustion concept [9]. The micro-combustion sites, supplied by the "H_2 Inlet" (fuel) and "Air 2 Inlet" (oxidizer), are annotated in Fig. 1. In this figure, the "Air 2 Inlet" is shown for clarity; however, in the physical burner it is located at a different cross-section due to

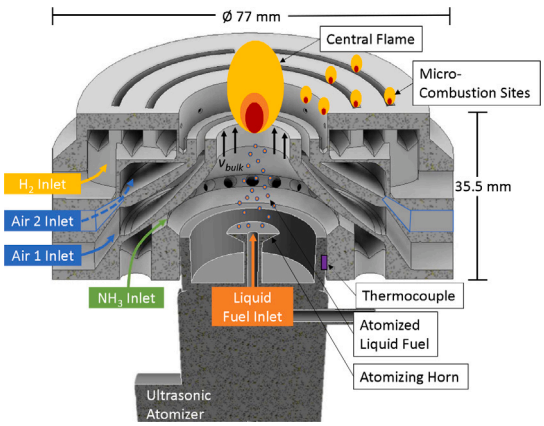

Fig. 1. Geometry of the fuel-flexible HyMAm-Flex (v18) burner with an ultrasonic atomizer, annotated with the bulk velocity, v_{bulk}, of the alcohol and NH_3 fuels.

spatial considerations. The second combustion strategy annotated in Fig. 1 consists of a central (NH_3–alcohol–air) flame. The NH_3–alcohol mixture enters the combustion zone through the central outlet, where v_{bulk} is annotated. The v_{bulk} is later defined in Section 3.3

An ultrasonic atomizer is employed for generating a spray of micrometer-sized droplets. The liquid alcohol enters the ultrasonic atomizer through the "Liquid Fuel Inlet", where it spreads across the surface of the atomizing horn and is atomized into a fine spray. Ammonia enters through the "NH_3 Inlet" and serves both as a fuel and as a carrier gas to transport the alcohol spray into the combustion zone. Within the combustion zone, the mixed NH_3 and alcohol spray interact with the oxidizer stream "Air 1 Inlet".

The complete burner design and geometry is presented by Kretzer et al. [29]. The burner body envelope measures 77 mm in diameter and 35.5 mm in height. To summarize, the key feature size parameters are as follows. For the central flame, the central outlet diameter is 14 mm. The air supply for the central flame is through an annulus with an 18.5 mm diameter and a slot width of 1.5 mm. For the micro-combustion sites, there are 3 rings, at diameters 28.2 mm, 41.2 mm, and 54.2 mm. The inner ring has 12 sites, the middle ring has 18 sites, and the outer ring has 24 sites. The air for each micro-combustion site is supplied coaxially to the combustion chamber through a 2 mm square hole. The hydrogen is supplied to the micro-combustion site through a ⌀1 mm orifice that is normal to the coaxial airflow, in the jet-in-crossflow configuration. Internal hydrogen supply lines to the hydrogen orifices have an effective diameter of 5.5 mm. The ultrasonic atomizer is positioned 24.6 mm from the combustion zone.

2.2. Simulation-guided additive manufacturing burner development

The burner design could only be realized through additive manufacturing, with numerical simulations guiding the development process. The design of the HyMAm-Flex (v18) burner was supported by numerical simulations with computational fluid dynamics in order to predict the flow and mixing characteristics and to find appropriate positions and dimensions of the supply channels for the three fuels and the air. The simulations were set up in the framework of the software package OpenFOAM. The computational domain with a wide range of physical scales inside the burner was discretized using a hexahedral-dominated structured mesh, comprising approximately 1.71 million cells. Simulations were carried out at an equivalence ratio of unity for all three fuels. The large-eddy simulations assessed the distribution of the fuels and the air inside the burner, as well as their mixing pattern. The present configuration and flow rates ensure the performance of the micro-mixing of H_2 with air in the upper burner region, as well as the central NH_3 flow carrying the fuel spray. Uniform delivery of H_2 to each of the micro-combustion sites, and uniform delivery of NH_3 and oxidizer to the combustion zone were demonstrated. Full details of the numerical methodology will be presented in future work.

Additive manufacturing enables the fabrication of complex geometries that would not be possible to achieve using conventional manufacturing techniques. Furthermore, AM allows materials to be selected to withstand the harsh conditions associated with the combustion environment. The HyMAm-Flex (v18) prototype was manufactured utilizing powder bed fusion of metal by using a laser beam (PBF-LB/M) [30]. PBF-LB/M is an established AM process for the direct production of metal components [31]. The process follows the characteristic layer-wise fabrication approach of AM [32]. Within an inert-gas atmosphere, a thin layer of metal powder is uniformly distributed onto a build platform with a recoater [33]. The laser beam selectively melts the powder according to the defined cross-sectional geometry. After exposure, the plate is lowered and a new layer of powder is applied [34]. This process is repeated until the component is complete. A Trumpf TruPrint 1000 system (TRUMPF Laser- und Systemtechnik GmbH, Ditzingen, Germany) with a focus diameter of 30 μ m and a maximum laser power of 200 W was used for production. IN718 was used as the material due to its high strength, temperature resistance up to approx. 700 °C, corrosion and oxidation resistance, and good weldability, which benefits processing in the PBF-LB/M process [35]. The prototype was manufactured using the following parameters: laser power 170 W, scanning speed 600 mm/s, layer thickness 30 μm, and hatch spacing 0.126 mm. The prototype was separated from the build platform by wire Electrical Discharge Machining (EDM) and then mechanically reworked on the functional surfaces. The external fixture was fabricated separately, with pipes brazed to the burner body.

2.3. Combustion experiments

Combustion experiments were performed in the ammonia combustion laboratory of the Engler-Bunte Institute at Karlsruhe Institute of Technology. Kretzler et al. [12] detailed the laboratory equipment and setup.

The physical burner is shown in Fig. 2. The schematic in Fig. 3 shows the branched supply lines for each of the gaseous fuels/oxidizer, which deliver the gases to four locations around the circumference of the burner; each line in this burner has an inner diameter of 4 mm to minimize line losses. This branched design ensures an equal split of the gas flows, providing uniform distribution to all four inlets to the burner. Providing the burner with an equal supply of gases to each inlet is important to ensure the micro-combustion sites create a uniform heating zone and ensuring that the ammonia carrier gas uniformly transports droplets to the combustion region.

In all experiments discussed, air was used as the oxidizer. The global equivalence ratio (ϕ), was unity for all experiments. To maintain controlled air supply to the fuels, and to enable exhaust gas measurements, a quartz glass cylinder with a diameter of 15 cm and a height of 20 cm was installed around the burner and sealed along the bottom. This geometry provided sufficient volume to contain the flame while preventing side-wall effects.

The gas flow rates are controlled using mass flow controllers (MFCs by Bronkhorst) with a relative accuracy of $< 0.5\%$. NH_3 (Air Liquide) with $> 99.98\%$ purity is used with gaseous H_2. For continuous gas flow, the liquefied NH_3 cylinders are maintained at room temperature using a heating system. In these experiments, ethanol absolute with $> 99.97\%$ purity is used as the carbon-neutral liquid fuel. Ethanol is used as the renewable liquid biofuel in place of methanol due to safety considerations. However, ethanol is a relevant and sustainable alternative fuel that can be employed as the low-carbon fuel in the various configurations. Despite differences in liquid viscosity, volatility, and evaporation rate, ethanol exhibits sufficiently similar atomization characteristics to methanol, and thus it does not fundamentally alter the

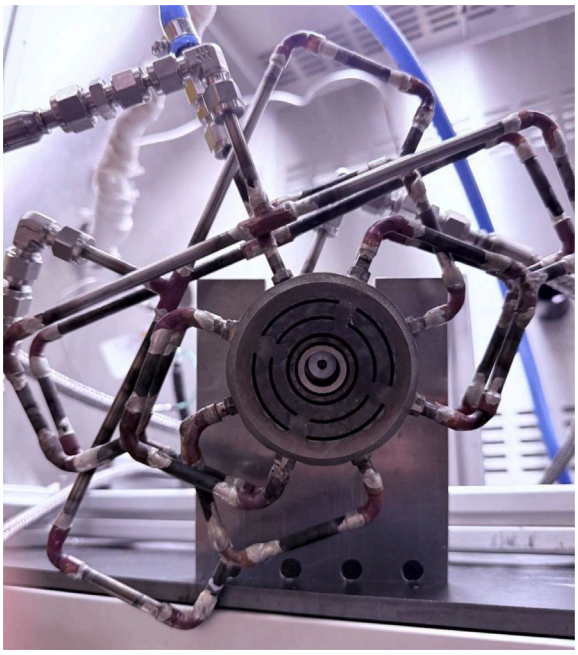

Fig. 2. Top view of the experimental research burner showing the branched design of gas flow supply lines into the burner from a single gas supply line.

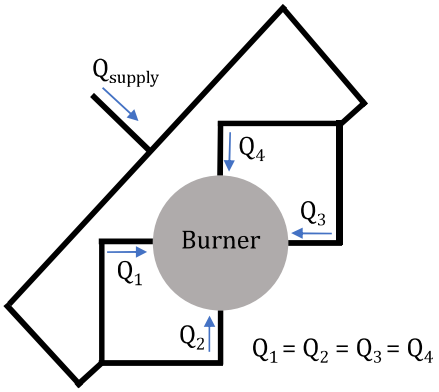

Fig. 3. Schematic of the branched design used to supply each gaseous fuel and oxidizer to the burner. This design ensures that the supply volumetric flow rate, Q_{supply}, is distributed evenly among the four burner inlets, such that Q_1=Q_2=Q_3=Q_4.

burner operation. Therefore, the use of ethanol represents a relevant and worthwhile fuel for this investigation. The liquid flow rate of the ethanol is controlled using a Teledyne 500D Syringe Pump. The flow accuracy of the liquid fuel supplied to the atomizer is within 0.5% of the set point.

Nitrogen-containing exhaust gas species were measured using the experimental setup described by Kretzler et al. [12]. A conical fixture was mounted on top of the quartz glass cylinder to channel the exhaust gases to a single sampling point, ensuring representative sampling. Exhaust gas measurements were recorded using a sampling probe with a diameter of 10 mm, and heated tubing to the gas analyzers was positioned directly at the burner outlet, centered in the conical device. The homogeneity of the exhaust gases was assessed at three positions within the outlet of the conical device, showing an average deviation of less than 11% across all species. Gas analyzers (ABB) were employed to measure nitrous oxide (N_2O) (0–500 ppmv, Uras 26) in the dry gas phase, whereas NH_3 (0–2000 ppmv, Limas21), NO (0–10000 ppmv, Limas21), and NO_2 (0–1000 ppmv, Limas21) were measured in the wet gas phase to prevent losses due to condensation. The measurement uncertainties were < 1.5% and the response times were < 4 s. Signal acquisition relied on an NI-9208 current-input module housed in an NI-DAQ-9179 chassis. In this work, all species were normalized to 15% O_2 following Baukal and Eleazer [36].

The species quantification is carried out using the characteristic emission wavelengths of excited species. The camera used EHD UV3528B with a UV lens, a focal distance of 25 mm, and an f-stop value of F2.8. The exposure time was set to 2.562 s and the gain was set to 900%. Two band-pass optical filters, BP324 and BP340 (Midwest Optical Systems Inc., Palatine, IL, USA), were placed in front of the lens to capture wavelengths between 300 and 400 nm, enabling the detection of OH* emission at 309 nm and NH* emission at 336 nm [37]. Thus, the recorded signal represents a superposition of the OH* and NH* emissions. The optical filters used for the transmission chemiluminescence measurements have a primary transmission band spanning 280–390 nm. The transmission at the NH* emission wavelength (336 nm) is 82%, while the transmission at the OH* emission wavelength (309 nm) is 63.5%, corresponding to the characteristic chemiluminescence bands discussed by Konnov [38]. Outside the primary transmission band, the optical density (OD) is greater than 3. While the optical filter (OD > 3) substantially suppresses broadband flame emission, residual background contributions, particularly in ammonia-containing flames, cannot be entirely excluded.

Two-dimensional projected images of chemiluminescence emissions may provide qualitative insight into the flame structure and behavior. Recent studies of NH_3–H_2 flames by Zhu et al. [39] show that hydrogen addition to NH_3 flames can significantly increase both OH* and NH* intensity, demonstrating that the signal depends strongly on chemical kinetics and overall reactivity. Furthermore, Zhu et al. [40] indicates that for NH_3–CH_4 flames, the OH* intensity may decrease with increasing NH_3 fraction and NH* intensity can exhibit a non-monotonic behavior with a maximum at intermediate NH_3 concentrations. In addition, ammonia combustion leads to lower adiabatic flame temperatures, which also affects chemiluminescence intensity independently of reaction rates. Recent studies by Karan et al. [41] indicate that NH* emission can be spatially correlated with regions of high heat release in ammonia flames. However, such relationships are fuel- and condition-specific and have not been universally validated. Consequently, comparisons across different fuel compositions and thermal powers are limited. In the present study, the chemiluminescence images are used as a qualitative indicator of the spatial location of the reaction zone and flame structure.

Chemiluminescence image analysis was performed in *MATLAB* [42] using threshold-based background subtraction, where pixels corresponding to the background were first identified and their mean intensity computed. All pixel values within this background intensity range were then set to zero, effectively isolating the flame front from the background.

An important consideration with alcohol–ammonia combustion is the potential formation of hydrogen cyanide (HCN), which is a highly toxic trace emission. Under the stoichiometric operating conditions investigated in the present study, this reaction pathway is considered unlikely, as HCN formation is typically associated with ultra-rich combustion conditions [43]. Therefore, HCN formation was not considered a substantial risk in the current experiments, but should be revisited in future experimental investigations.

2.4. Ultrasonic atomization

A key feature of the burner's design is the integration of an ultrasonic atomizer, which is used to generate the fine spray of the liquid, carbon-containing fuel since it provides a low initial spray velocity, a narrow size distribution largely insensitive to small changes in the input flow rate, and droplet formation without co-flow or high injection pressure. Sprays were produced by the ultrasonic atomizer used in

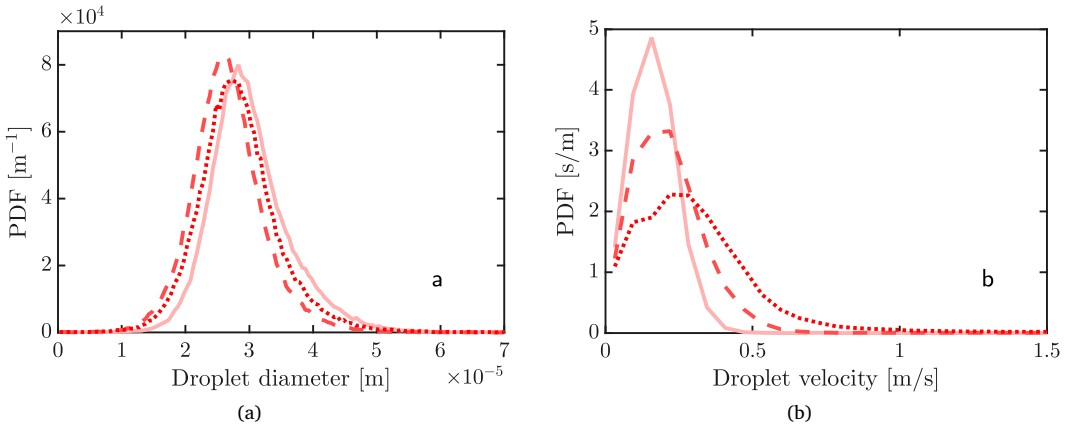

Fig. 4. Probability density distributions of (a) size and (b) velocity for droplets produced by ultrasonic atomization for ethanol measured at an axial distance of approximately 1 mm downstream of the atomizing horn for volumetric flow rates of 0.05 mL/s (solid line), 0.10 mL/s (dashed line), and 0.17 mL/s (dotted line).

this design (Lechler, Model AV-710.061.41.40). Ultrasonic atomization occurs when a liquid film on the vibrating surface undergoes destabilization known as the Faraday instability. This causes surface waves to be generated that eject droplets once a critical amplitude is reached. The resulting spray velocity is induced by destabilization of the liquid film by the vibrating surface. Liquid is supplied to the atomizing horn through a central bore, shown in Fig. 1, with negligible pressure drop. The atomizer operates at 58 kHz and has an aluminum body that has a diameter of 30 mm and a length of 78 mm. The atomizing horn, shown in Fig. 1, is 10 mm in diameter.

The sprays were characterized via Phase-Doppler Anemometry (PDA) by Morse et al. [44]; results are shown in Fig. 4. Here, the size and velocity distributions for ethanol droplets produced at various flow rates (0.05–0.17 mL/s) are measured at an axial distance of approximately 1 mm downstream of the atomizing horn. Droplet characterization was performed outside the combustion environment and outside the burner body, under ambient conditions (20 °C, 1 atm). With the atomizer positioned at an offset from the combustion zone, droplet evaporation created by the hot reaction region is limited. This configuration provides conditions that are more comparable to the cold-flow environment in which the atomizer was characterized. The PDA measurements provide the burner inlet boundary conditions, beyond which the spray velocity will be largely influenced by the carrier gas. The complex carrier-gas flow within the burner body requires numerical characterization to provide velocity profiles, motivating ongoing and future studies.

Because the atomizer contains a piezoelectric transducer, it must operate below its Curie temperature. According to the manufacturer's specifications, this limit is 135 °C. Since flame temperatures well exceed this temperature, the burner was designed to offset the atomizer from the combustion chamber. In addition to the design of the burner, additional precautions were taken to keep the atomizer cool, including the use of insulation to isolate the atomizer from the burner body, active water cooling, and passive cooling from a carrier gas. The temperature of the atomizer was continuously monitored using a thermocouple in the threaded area of the atomizer shown in Fig. 1.

3. Results and discussion

The primary objective of the present study is to provide an initial experimental characterization of the burner concept and its fuel flexibility. The results of the additive manufacturing process and a discussion on the integration of numerical simulations and their contribution to the selection of appropriate operating conditions are discussed first. Later in this section, chemiluminescence images in combination with visible flame luminosity are used to qualitatively assess reaction-zone structure and discuss flame stability. Exhaust gas measurements of ternary-fuel combinations are later used to quantitatively baseline the burner's nitrogen-containing emissions and provide insight into the completeness of the combustion.

3.1. Numerical simulations

The numerical simulations were essential in achieving functional fluid-dynamic behavior within the internal fuel passages of the burner without requiring fabrication and experimental characterization of every burner iteration. In particular, early simulations of previous versions of the HyMAm-Flex, which were never experimentally characterized, showed issues associated with the internal hydrogen supply to the micro-combustion sites. These findings were essential to design the geometry of the supply channels and the appropriate hydrogen supply rate required to maintain a uniform fuel supply and a positive pressure drop across the 54 hydrogen orifices. Furthermore, the simulations identified operating conditions that produced recirculation zones within the burner, which may influence spray distribution within the combustion zone. This information can therefore be used to limit such operating conditions and promote a more homogeneous spray distribution, thereby reducing localized hot-spot formation, which is relevant for the burner emissions.

3.2. Additive manufacturing

The benefits of additive manufacturing (AM) for this specific burner are manifold. AM allows quick iterations on designs, paired with flexibility for accommodating different boundary conditions when required. This is demonstrated by the HyMAm-Flex burner, where PBF-LB/M enables the realization of a monolithic burner architecture consolidating multiple subsystems into a single component. This monolithic design includes fine hydrogen micro-channels, internal air distribution networks, and the integration of the ultrasonic atomizer for liquid fuel atomization [29].

Such features would be difficult or unfeasible to achieve through conventional subtractive or formative manufacturing methods. A monolithic design reduces tolerance stacks, alignment errors, and sealing interfaces that would otherwise be introduced in a modular design. For micro-mix combustion systems, where flow uniformity across many small combustion sites is important, reducing tolerance accumulation is particularly beneficial. Additionally, by eliminating thermally sensitive joining interfaces, such as brazed connections, the monolithic AM design improves structural integrity under the cyclic thermal loading characteristic of combustion environments. In this way, AM did not merely replicate what conventional manufacturing offers. It largely

expands the possible design space, allowing the geometry to be driven by the physical requirements of multi-fuel combustion rather than by manufacturing constraints.

The applied Design for Additive Manufacturing (DfAM) strategy allowed the burner body to be produced with minimal support structures. However, powder removal from fine internal channels remained a challenge. Despite small process-related distortions, submersion testing and endoscopic inspection confirmed complete patency of all hydrogen outlets, underscoring the robustness of the DfAM approach. Three-dimensional scanning confirmed the high dimensional accuracy on outer surfaces while locally increased deviations were identified in geometrically complex interior regions of the burner with maximum deviations between 0.1 and 0.3 mm [29]. Although the largely closed geometry prevents direct measurement of the surface roughness in the internal passages, the surface roughness for internal passages and overhang areas is expected to be no more than 0.02 mm on average. To reduce the sensitivity of the burner to such manufacturing imperfections, the internal flow passages were designed such that the dominant pressure losses occur at the inlet to the combustion zone rather than within the internal distribution network. The performance of the realized burner design is discussed further in Section 3.3.4.

3.3. Fuel flexibility

The burner can operate under multiple fueling configurations without requiring the simultaneous supply of all fuels. Single-, dual-, and ternary-fuel operating conditions are investigated by systematically varying the fuel flow rates to characterize burner performance and explore the operating parameter space. The initially investigated configurations using visible flame luminosity and chemiluminescence imaging are summarized in Table 1.

Provided in Table 1 are the fuel supplies, reported in terms of the energy fraction, energy percentage, and fuel flow rate. Additionally reported are the figures in which these configurations appear and the bulk velocity v_{bulk} of the fuel through the central outlet, depicted in Fig. 1. The material data of the fluids at ambient conditions are provided in Table 2. The bulk velocity is calculated by $(Q_{NH_3} + Q_{eth})/A_{cen}$, where Q_{NH_3} and Q_{eth} are the volumetric flow rates of ammonia and ethanol, respectively, and A_{cen} is the cross-sectional area of the central outlet. The Reynolds number $Re = v_{bulk} l_{char} \rho/\mu$ for the central outlet was approximated using the bulk velocity through the central outlet, the central outlet diameter (14 mm) as the characteristic length scale l_{char}, and the dynamic viscosity μ of ammonia gas. Similarly, the Reynolds number for the micro-combustion sites was calculated using the total volumetric flow through the 54 micro-combustion sites, the averaged viscosity of the hydrogen–air mixture, and the width of the micro-combustion site. For all cases, the Reynolds number at the micro-combustion sites remained below unity.

Visible flame luminosity and chemiluminescence images are used to evaluate flame structure and stability for the various fuel combinations. This qualitative analysis provides an initial assessment of burner fuel flexibility and identifies limitations in the burner geometry that require further design iteration.

3.3.1. Single-fuel configurations

The single-fuel configurations include C_2H_5OH and H_2 flames, shown in Fig. 5. Both configurations produced stable flames without flame blow-off. For the C_2H_5OH configuration, the atomizer generates the spray within the burner body, while the low-pressure region created by the coaxial air supply for the central flame draws the droplets into the combustion zone. The resulting flame is shown in Fig. 5(a), which is shown to not be symmetric. A slight misalignment of the atomizer within the burner body produced the asymmetric flame structure, which is also observed in subsequent ethanol-containing flames. The H_2 micro-combustion concept is shown in Fig. 5(b). An orange coloration of the hydrogen flame was consistently observed at the highest hydrogen thermal power (1.4 kW) across all fuel combinations (including hydrogen alone) and is therefore not believed to originate from the flame chemistry itself. The H_2 forms a symmetric conical flame surrounding the central outlet through which NH_3 and C_2H_5OH are introduced in later configurations. These micro-combustion sites operate independently of the central flame and can therefore be adjusted separately to achieve the desired thermal load. During this experimental campaign, the H_2 power was varied between 0.5 and 1.4 kW. The lower limit ensured sufficient fuel supply to overcome internal line losses. The upper limit was intended to constrain the flamelet width, thus minimizing interactions between neighboring flamelets. Limiting flamelet interaction was important for controlling H_2 flame temperature, maintaining flamelet stability, protecting the ultrasonic atomizer from excessive heat transfer, and reducing NO_x formation when later introducing NH_3.

In the chemiluminescence images, note that some imaging artifacts are observed, which can be ignored. First, a faint circular pattern appears in the background of the flame, which is also present in later images of the flame; this is an artifact of the test bench enclosure. Reflections from the burner body near the base of the flame and from the alignment bolts used to center the quartz glass chamber are visible. These features are solely imaging artifacts and do not correspond to any physical structures within the flame.

Table 1
Operating conditions for Cases 1-14 with $\phi = 1$. The energy fraction and volumetric flow rate for each case are provided in parentheses and square brackets, respectively.

Ca. #	H_2	NH_3	C_2H_5OH	Fig. #	v_{bulk} (ms^{-1}) [Re]
1	0 kW (0%) [0 lpm]	0 kW (0%) [0 lpm]	0.54 kW (100%) [1.5 mL/min]	5(a)	<0.01 [0]
2	1.4 kW (100%) [7.95 lpm]	0 kW (0%) [0 lpm]	0 kW (0%) [0 mL/min]	5(b), 9(a)	0 [0]
3	1.4 kW (44%) [7.95 lpm]	0 kW (0%) [0 lpm]	1.8 kW (56%) [5 mL/min]	6(a), 8(a), 9(d)	<0.01 [0]
4	0 kW (0%) [0 lpm]	0.2 kW (10%) [0.80 lpm]	1.8 kW (90%) [5 mL/min]	6(b)	0.08 [80]
5	1 kW (80%) [5.64 lpm]	0.25 kW (20%) [1.05 lpm]	0 kW (0%) [0 mL/min]	7(a)	0.10 [110]
6	1 kW (76%) [5.64 lpm]	0.32 kW (24%) [1.29 lpm]	0 kW (0%) [0 mL/min]	7(b)	0.12 [130]
7	1 kW (72%) [5.64 lpm]	0.38 kW (28%) [1.58 lpm]	0 kW (0%) [0 mL/min]	7(c)	0.15 [160]
8	1 kW (68%) [5.64 lpm]	0.48 kW (32%) [1.98 lpm]	0 kW (0%) [0 mL/min]	7(d)	0.19 [200]
9	1.4 kW (34%) [7.95 lpm]	1 kW (23%) [4.10 lpm]	1.8 kW (43%) [5 mL/min]	8(b), 9e	0.39 [410]
10	1.4 kW (27%) [7.95 lpm]	2 kW (38%) [8.30 lpm]	1.8 kW (35%) [5 mL/min]	8(c), 9(f), 10(c)	0.78 [840]
11	1.4 kW (24%) [7.95 lpm]	2.5 kW (44%) [10.30 lpm]	1.8 kW (32%) [5 mL/min]	8(d)	0.97 [1040]
12	1.4 kW (59%) [7.95 lpm]	1 kW (31%) [3.96 lpm]	0 kW (0%) [0 mL/min]	9(b)	0.37 [400]
13	1.4 kW (40%) [7.95 lpm]	2.1 kW (60%) [8.72 lpm]	0 kW (0%) [0 mL/min]	9(c),10(b)	0.82 m/s [880]
14	0 kW (0%) [0 lpm]	0.3 kW (14%) [1.20 lpm]	1.8 kW (86%) [5 mL/min]	10(a)	0.11 [120]

Table 2
Material data of the fluids at ambient conditions.

Fluid	Density, ρ [kg/m^3]	Dynamic Viscosity, μ [Pa s]
NH_3	0.73	9.8×10^{-6}
H_2	0.084	8.9×10^{-6}
C_2H_5OH	789	1.07×10^{-3}
Air	1.20	1.81×10^{-5}

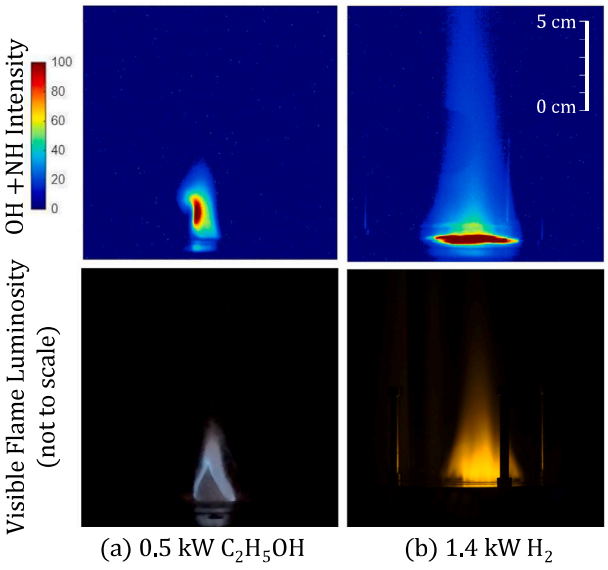

Fig. 5. Single-fuel, (a) C_2H_5OH (Case 1) and (b) H_2 (Case 2) flame. The chemiluminescence and visible flame images are not recorded at the same time instant and are recorded from different camera angles.

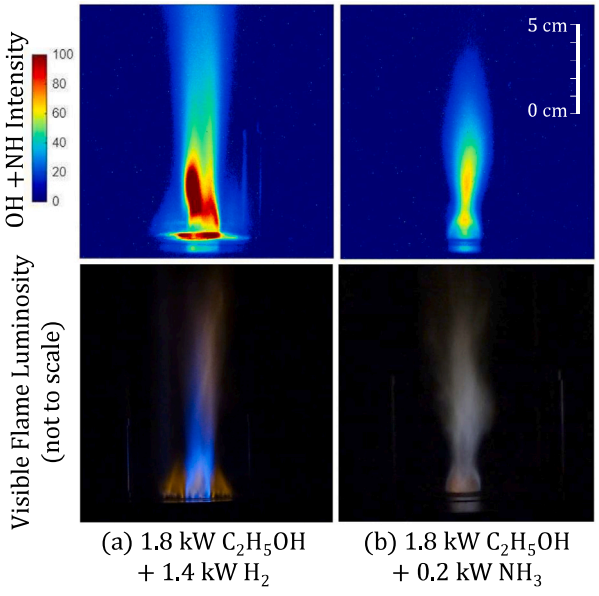

Fig. 6. Dual-fuel, (a) C_2H_5OH–H_2 (Case 3) and (b) C_2H_5OH–NH_3 (Case 4) flame. The chemiluminescence and visible flame images are not recorded at the same time instant and are recorded from different camera angles.

3.3.2. Dual-fuel configurations

The burner was also operated under dual-fuel conditions. Dual-fuel configurations involving alcohol are shown in Fig. 6. Both flames remained stable without flame blow-off. The C_2H_5OH–H_2 flame in Fig. 6(a) shows the H_2 micro-combustion flamelets forming a thermal dome at the base of the elongated central flame. The C_2H_5OH–NH_3 flame is shown in Fig. 6(b). The base of the flame remains attached to the burner body and exhibits a visible orange hue. The flame structure shown in the chemiluminescence images shows that the reaction zone is nearly splitting due to the high strain in the flame, causing visible necking. If this reaction zone becomes split and discontinuous, it can lead to incomplete combustion of the fuels.

The carbon-free dual-fuel configurations are shown in Fig. 7. In Cases 5–8, increasing NH_3 flow rates were added to an H_2 flame. The corresponding chemiluminescence intensity and visible flame luminosity images are shown in Fig. 7. In the visible flame images, the hydrogen micro-combustion flamelets, at a lower thermal load than has been shown previously, are largely invisible. In the chemiluminescence images for the lower NH_3 flow rates, shown in Figs. 7(a) and (b) (Cases 5 and 6), the reaction zone remains attached to the burner. At higher NH_3 flow rates, shown in Fig. 7(c) and 7(d) (Cases 7 and 8), the reaction zone lifts off from the burner body. The increased flame strain produces the necking structure clearly visible in Fig. 7(d) chemiluminescence image. This necking behavior is also visible in the visible flame images, where increasing NH_3 flow rates cause the flame to further lift off from the burner body and increase in height. The visible flame height for these cases remained below 10 cm. Cases 5–8 maintained stable operation, with ammonia slip below 15 ppmv within the sealed test chamber and no flame extinction.

3.3.3. Ternary-fuel configuration

Cases 9–11 correspond to H_2–NH_3–C_2H_5OH operation with progressively increasing NH_3 flow rates. The corresponding chemiluminescence intensity and visible flame luminosity images are shown in Fig. 8(a)–(d). These flames appear elongated, with flame heights exceeding 20 cm. Beginning with the first column of Fig. 8, the H_2–C_2H_5OH flame (Case 3) exhibits the asymmetry due to misalignment of the ultrasonic atomizer. Nevertheless, the atomized ethanol reached the combustion zone and the high-intensity region remains near the burner body. The addition of NH_3 in Fig. 8(b) (Case 9) stretches the flame and lifts the high-intensity region away from the burner body. In Figs. 8(c) and (d) (Cases 10 and 11, respectively), the reaction zone extends beyond the field of view of the chemiluminescence camera. Figs. 8(a)–(c) (Cases 3, 9, and 10) remained stable with ammonia slip below 15 ppmv within the test chamber and without flame extinction. In contrast, the operating conditions for Case 11 (Figs. 8(d)) produced unstable operation and incomplete NH_3 combustion, producing ammonia slip levels above 15 ppmv within the test chamber. In the visible flame images, increasing NH_3 flow rates lead to increased flame height, which may be associated with the slower burning rate of NH_3. This may also be attributed to the laminar operating regime of the central flame near the nozzle exit, which does not promote air–fuel mixing. However, for the present burner geometry, achieving turbulent flow conditions for the central outlet nozzle exit was not feasible.

The differences between the carbon-free dual-fuel combustion strategy and the ternary-fuel combustion strategy are further examined in Fig. 9 through the chemiluminescence images. In this figure, the top row shows the carbon-free, dual-fuel operating conditions and the bottom row shows the ternary-fuel operating conditions under nearly identical contributions of the carbon-free fuels for each column, where the main difference is the 1.8 kW energy fraction contribution from the C_2H_5OH. The columns from left to right show an increasing energy fraction contribution from the NH_3.

Under the carbon-free, dual-fuel operating conditions, increasing NH_3 causes the flame to lift-off from the burner and the high-intensity region to move downstream. This behavior is visible in both the chemiluminescence and visible flame images. In Fig. 9(c), this high-intensity region lifts off entirely. For the carbon-free, dual-fuel configurations, there is no mechanism to stabilize the central flame, which is entirely laminar at the nozzle exit based on the Reynolds numbers shown in Table 1. The case shown in Fig. 9(c) corresponds to visible flame which is later shown in Fig. 10(b).

In the bottom row of Fig. 9, where C_2H_5OH is present, the same trend of increased NH_3, causing the reaction zone to move downstream, is also observed. However, under these operating conditions, the C_2H_5OH stabilizes the core of the flame, thereby avoiding the detachment of the reaction zone and allowing for the stable operation in Fig. 9(f), which corresponds to the visible flame luminosity which is later shown in Fig. 10(c).

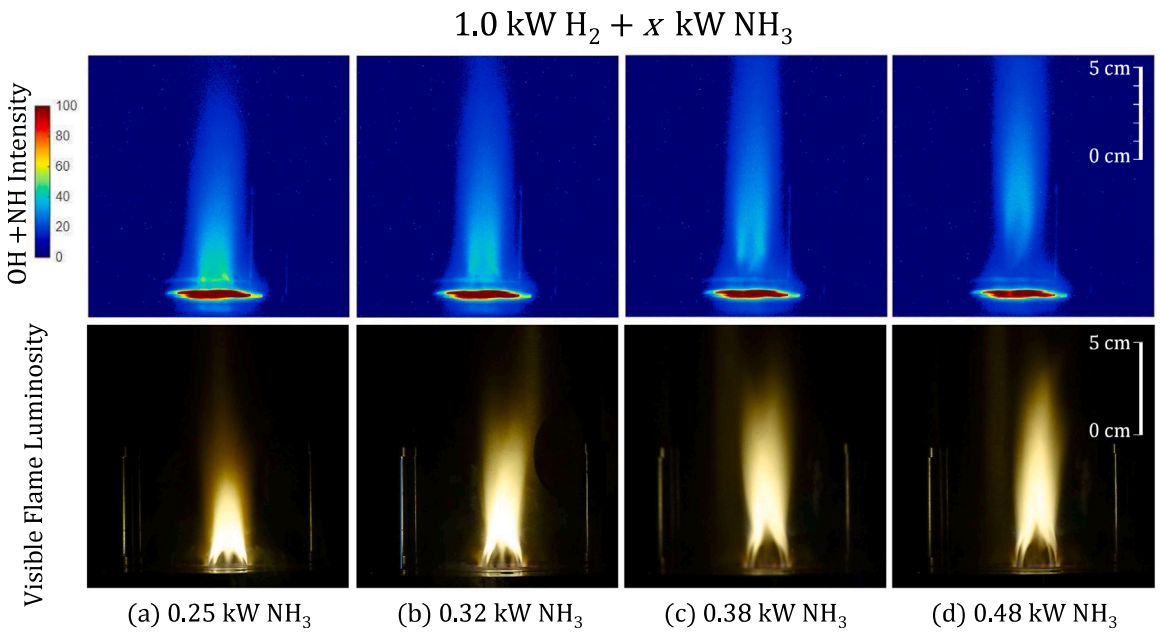

Fig. 7. Chemiluminescence intensity and visible flame luminosity for H_2–NH_3 flame, showing increasing contributions of NH_3 (Cases 5–8, respectively). The chemiluminescence and visible flame images are not recorded at the same time instant and are recorded from different camera angles.

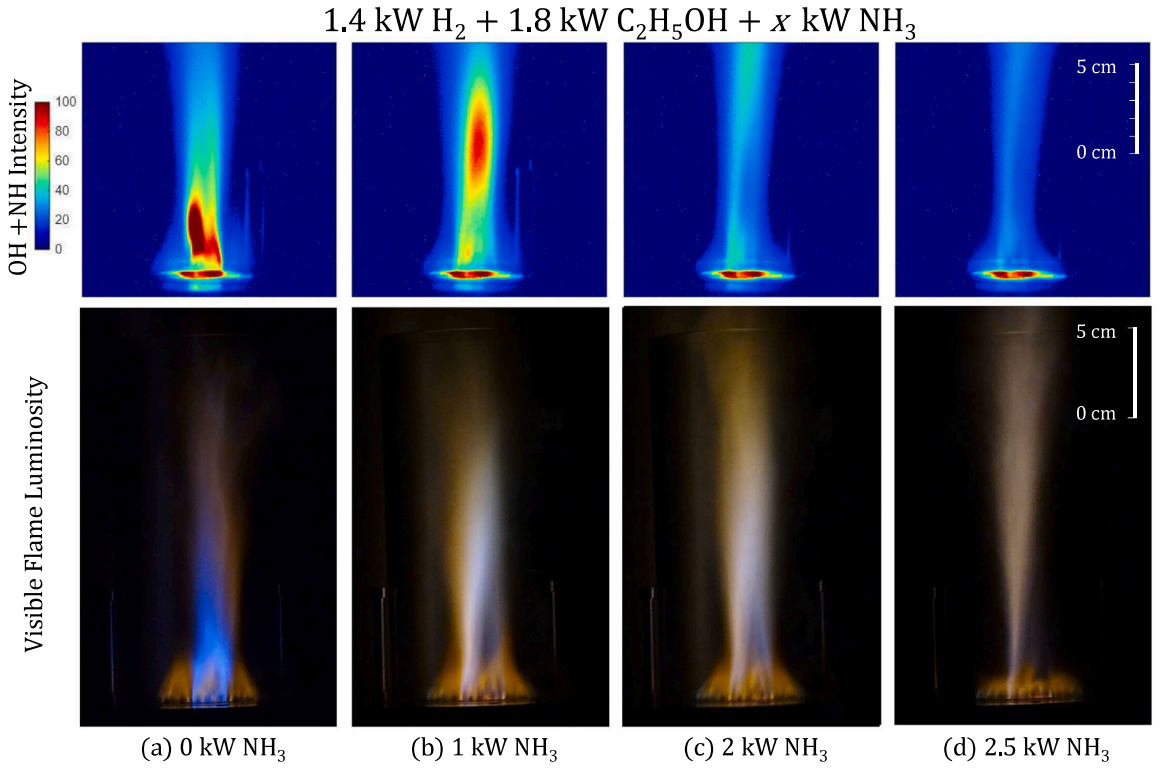

Fig. 8. Chemiluminescence intensity and visible flame luminosity for H_2–NH_3–C_2H_5OH flame, showing increasing contributions of NH_3 for Cases 3, 9, 10, and 11, respectively. The chemiluminescence and visible flame images are not recorded at the same time instant and are recorded from different camera angles.

For the H_2–NH_3–C_2H_5OH flame, a stable flame was achieved up to and including energy fractions of 27% H_2, 38% NH_3, and 35% C_2H_5OH (Case 10). The bulk velocity of the central NH_3–C_2H_5OH flame for these values reached 0.78 m/s, where Re = 840. Attempts to increase the NH_3 content beyond this value led to high values of ammonia slip for the case with energy fractions of 24% H_2, 44% NH_3, and 32% C_2H_5OH (Case 11), which produced a bulk velocity of 0.97 m/s, where Re = 1040. Both flames are likely to be laminar near the flow exiting the central outlet, where the limited turbulent mixing within the central outlet likely contributed to the incomplete NH_3 combustion and resulting ammonia slip.

3.3.4. *Limitations to fuel flexibility*

Finally, the limitations of the various fuel combinations are discussed for the HyMAm-Flex (v18). Representative visible flames from different operating conditions are shown in Figs. 10(a)–(c). Shown here

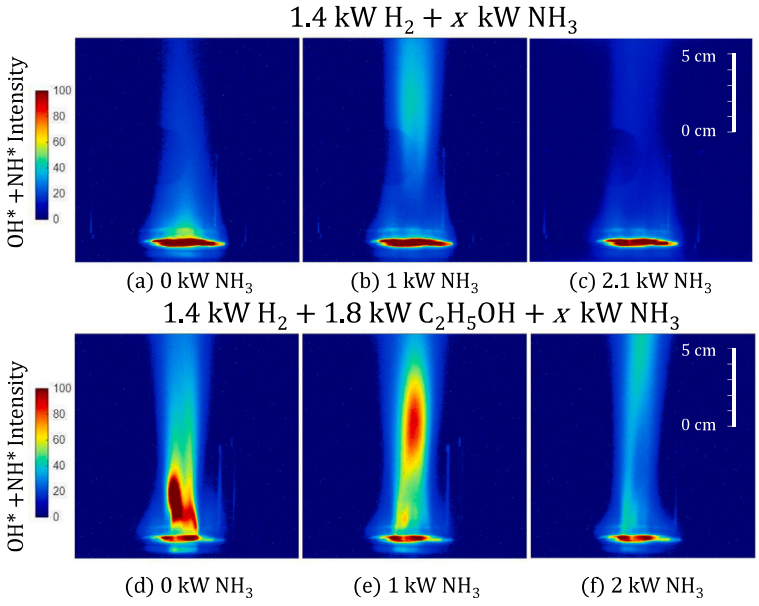

Fig. 9. Chemiluminescence intensity images of (a-c) H_2-NH_3 flame and (d-f) H_2-NH_3-C_2H_5OH flame, showing increasing contributions of ammonia. The shown cases are (a) 2, (b) 12, (c) 13, (d) 3, (e) 9, and (f) 10.

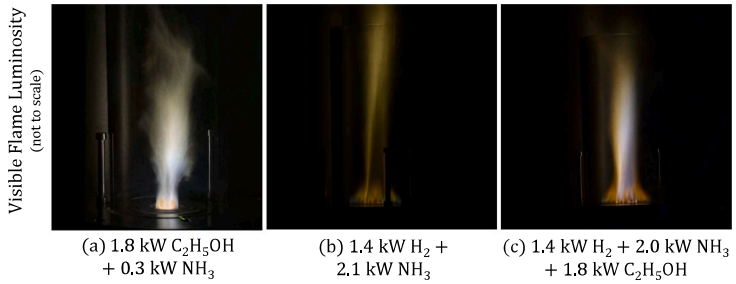

Fig. 10. Visible flame luminosity of the various flame types. The shown cases are (a) 14, (b) 13, and (c) 10.

is an NH_3–C_2H_5OH flame, an H_2–NH_3 flame, and an H_2–NH_3–C_2H_5OH flame, respectively.

The NH_3–C_2H_5OH flame shown in Fig. 10(a) corresponds to a slightly higher NH_3 flow rate than the stable condition shown in Fig. 6(b), but could not sustain stable combustion. This instability is likely associated with the narrowing flame waist discussed previously, which causes pinch-off of the upper reaction zone and results in NH_3 slip. Additional stabilization mechanisms are therefore required for the central flame.

Fig. 10(b) (Case 13) shows a long H_2–NH_3 flame with a visible hollow core. In spite of the H_2 micro-combustion sites creating a hot annulus around the central flame, this heated zone is not sufficient to penetrate the core. The hollow structure indicates a high concentration of unburned fuels in the center, leading to NH_3 slip. The elongated shape of the flame pictured in Fig. 10(b) is consistent with the slow burning rate of NH_3. The flame is incapable of achieving satisfactory NH_3 combustion and is therefore not considered a stable operating condition. Notably, combustion at the periphery of the central flame remains sustained at the high bulk velocity (0.82 m/s), while the unburned core of the flame contributes to the high ammonia slip. This indicates that the burner performance could be improved by enhanced mixing within the central flame.

In contrast to the two previously described unstable flames, the H_2–NH_3–C_2H_5OH flame in Fig. 10(c) remains stable. In this case, the C_2H_5OH flow rate is comparable to that in Fig. 10(a), while H_2 and NH_3 are supplied at rates similar to those in Fig. 10(b). The combination of the three fuels, however, enables flame stabilization. At a bulk velocity similar to that in Fig. 10(b), Fig. 10(c) shows a flame with a stably burning core.

This section demonstrated the fuel flexibility of the HyMAm-Flex (v18) burner. Several observations can guide future improvements to burner performance and fuel flexibility. For the single-fuel configurations, improved alignment of the ultrasonic atomizer is required to ensure a uniform and symmetric ethanol spray distribution. For the dual-fuel configurations, improved air–fuel mixing within the central flame is necessary to promote complete ammonia combustion.

Given the current burner geometry and under the present operating conditions, the central flame remained laminar at the nozzle exit (central outlet), shown in Table 1, and ethanol alone could not fully stabilize the NH_3 flame. Increasing turbulent mixing within the central outlet may therefore improve flame stabilization. This can be achieved by increasing the bulk velocity through the central outlet of the burner, or adding small features such as tabs or serrations to increase the mixing of the fuel and oxidizer. A final key observation from the ternary-fuel configurations was that the hot-zone created by the micro-combustion flamelets did not sufficiently penetrate the core of the central flame. This limitation could potentially be addressed by arranging the micro-combustion sites on a conical surface rather than the current flat plane. These proposed modifications to the burner geometry could improve the fuel flexibility of the burner without significantly altering the overall architecture, which remains suitable for further study.

Despite the misalignment of the integrated ultrasonic atomizer, which introduced an asymmetry in the C_2H_5OH supply within the

Table 3
Additional operating conditions used for measuring exhaust gas, where $\phi = 1$. The energy fraction and volumetric flow rate for each case are provided in parentheses and square brackets, respectively.

Ca. #	H_2	NH_3	C_2H_5OH	Fig. #	v_{bulk} (ms^{-1}) [Re]
15	0.60 kW(46%) [3.38 lpm]	0.15 kW(12%) [0.63 lpm]	0.54 kW(42%) [1.5 mL/min]	–	0.06 [60]
16	0.60 kW (45%) [3.38 lpm]	0.20 kW (15%) [0.83 lpm]	0.54 kW (40%) [1.5 mL/min]	12(a)	0.08 [80]
17	0.60 kW (40%) [3.38 lpm]	0.20 kW (13%) [0.83 lpm]	0.72 kW (47%) [2 mL/min]	12(b)	0.08 [80]
18	0.60 kW (32%) [3.38 lpm]	0.20 kW (10%) [0.83 lpm]	1.10 kW (58%) [3 mL/min]	12(c)	0.08 [80]

burner, the visible flame and chemiluminescence images of the H_2 micro-combustion sites appeared relatively uniform in size and intensity, while the NH_3–H_2 flames remained largely symmetric. This suggests that the burner is relatively insensitive to the small manufacturing deviations previously noted. Based on the design limitations presented, future numerical studies will include targeted investigations into mechanisms to improve turbulent mixing of the central flame, thereby enhancing flame stability. While standard manufacturing practices would demand a considerable amount of effort and ultimately more compromises to integrate the suggested revisions to the burner design, with AM the aforementioned modifications to the geometry are largely unlimited compared to conventional manufacturing. A revised AM model addressing the modifications can be readily realized, and numerical simulations can begin assessing if the targeted metrics for this burner version are achieved.

3.4. Exhaust gas measurements

In order to complete a baseline assessment of the burner performance under ternary-fuel operating conditions, flue gases were to be examined. As previously mentioned, the ternary fuel operating conditions resulted in an elongated flame. In order to restrict the length of the flame for the test bench, lower thermal loads were considered for the exhaust gas measurement configurations.

Four additional operating conditions are presented in Table 3, with the corresponding exhaust gas measurements for each case shown in Fig. 11. The reported measurements in Fig. 11 represent the time-averaged value over the two-minute sampling period of the ABB gas analyzer, and the standard deviation represents the fluctuations in the measured value under identical operating conditions.

The three columns plotted for each operating condition in Fig. 11, correspond to ammonia slip, NO_x emissions, and N_2O emissions, respectively. Across Cases 15-18, NO_x emissions remain between 360 and 400 ppmv (wet). Ammonia slip levels remained comparatively low, between 10-18 ppmv (wet). N_2O values had the most variation between cases, varying between 14 and 32 ppmv (dry). Here, the measurements are normalized to 15% O_2 in the air [36].

In Cases 15 and 16, an attempt was made to isolate the effect of introducing more NH_3, while holding H_2 and C_2H_5OH flow rates constant. The thermal heating from the micro-combustion sites remains constant for the two cases. As previously discussed qualitatively, increasing the NH_3 supply appears to reduce the combustion intensity in the central flame, which is consistent with conditions typically associated with lower flame temperatures. The findings shown between Cases 15 and 16 seem to confirm this behavior, showing that the N_2O value significantly increases with the introduction of more NH_3. Elevated N_2O formation is commonly associated with lower-temperature ammonia oxidation pathways [45]. This is accompanied by an increase in ammonia slip. Together, this indicates that enhanced mixing of the ammonia is needed to promote better mixing and combustion characteristics. One possible approach for mitigating N_2O emissions

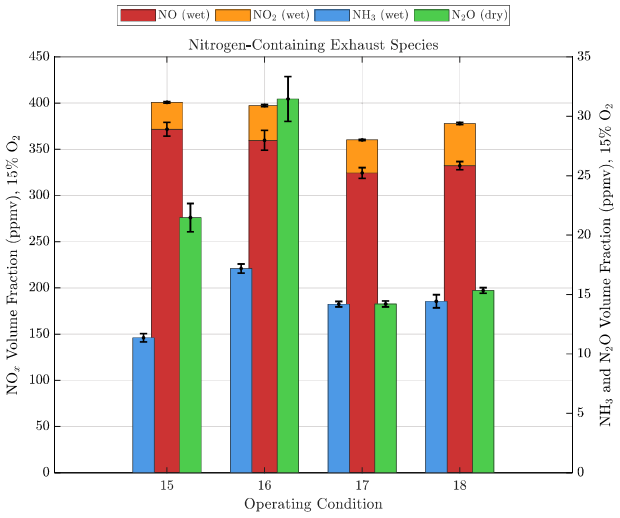

Fig. 11. Nitrogen-containing gas species for the operating conditions in Table 3.

is to reduce flame heat losses, which may be enhanced by the ambient conditions in the current test chamber. While these conditions were considered in the present study to limit experimental variables, they are not fully representative of a true combustion environment. In future work, improved insulation surrounding the combustion zone and a hot-gas co-flow could be introduced to better replicate realistic conditions.

Under operating conditions 16–18, the influence of increasing the C_2H_5OH content is evaluated while keeping the H_2 and NH_3 flow rates constant. While increasing the C_2H_5OH content and holding the other fuel flow rates constant, Table 3 shows that the bulk velocity through the central outlet remains constant. To maintain an equivalence ratio of unity, however, the coaxial air supply for the C_2H_5OH–NH_3 flame is increased independently as the C_2H_5OH flow rate is increased. The influence of the increased coaxial air flow on the central flame, while maintaining a constant bulk velocity of the fuels through the central outlet, is shown in Fig. 12. As the coaxial air velocity increases, the central flame appears increasingly elongated. In addition, the fuel composition also changes. As noted in Table 3, increasing the C_2H_5OH supply corresponds to a lower ammonia energy fraction in the fuel mixture. The NH_3 energy fraction decreases from 15% in Case 16 to 13% in Case 17 and 10% in Case 18, corresponding to a 5% reduction of its total energy contribution between Cases 16 and 18. Thus, several factors change simultaneously with increasing ethanol addition, including changes in fuel composition and local flow conditions. Cases 16–18 correspond to the chemiluminescence images in Fig. 12(a)–(c), respectively. Comparing Cases 16 and 17, there is a decrease across all nitrogen-containing exhaust species with increasing C_2H_5OH content. Notably, the N_2O and NH_3 values decrease in Case 17 compared to Case 16. The increased coaxial air supply may improve local mixing, while the additional ethanol content may promote flame stabilization and ammonia conversion. Consequently, the observed emissions trends likely result from a combination of changes in fuel composition and flow conditions. Comparing Cases 17 and 18, further addition of C_2H_5OH slightly increases N_2O and NO_x emissions, while ammonia slip remains nearly unchanged. In the literature, wherein NH_3-based combustion systems blended with highly reactive fuels, NO formation can exhibit a non-monotonic dependence on fuel composition, implying the existence of an optimal blend ratio that minimizes NO emissions [46]. In the present study, while the N_2O and NO_x emissions remain substantially lower than those recorded in Case 16, these results suggest that the emissions reductions associated with increasing C_2H_5OH addition may diminish beyond a certain ethanol content. This finding is in

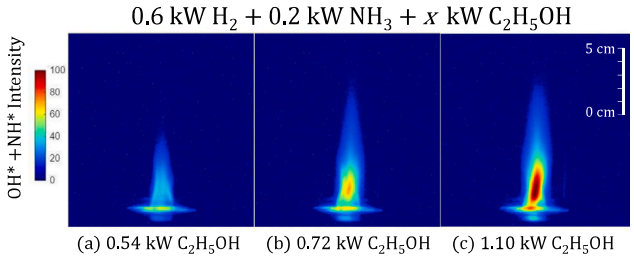

Fig. 12. Chemiluminescence intensity of H_2–NH_3–C_2H_5OH flame showing increased contributions of C_2H_5OH from (a) to (c). The shown cases are (a) 16, (b) 17, and (c) 18.

agreement with what was observed in Section 3.3.4 regarding the diminishing benefit of alcohol addition to stabilize the central flame.

3.5. Ultrasonic atomization

The burner with the atomizer was safely tested for thermal loads up to 5.7 kW with measured temperatures of the atomizer case never exceeding 57 °C. Thus, it was possible to effectively cool the atomizer with thermal shielding, active cooling, and the passive cooling of the NH_3.

The droplet size was largely insensitive to small changes in the liquid fuel flow rate, while the droplet velocity increased with increasing flow rate but did not scale proportionally. The burner design therefore provides considerable flexibility for a wide range of liquid fuels.

Under the ternary-fuel operating conditions considered in Table 1 (Cases 9–11), the estimated droplet residence times are between 3 and 6 ms. It is therefore expected that the carbon-based fuel remains primarily in the liquid phase until reaching the combustion zone. However, the smallest droplets in the spray may evaporate and the remaining droplets may reduce in size. In contrast, under the operating conditions considered in Table 3 (Cases 15–18), the estimated residence times increase to between 300 and 400 ms. Under these operating conditions, partial evaporation of the alcohol droplets is expected prior to reaching the combustion zone. For these operating conditions, as shown in Fig. 12, the chemiluminescence emission shows an increase with increasing C_2H_5OH flow rate. This trend is consistent with an increased contribution of C_2H_5OH to the reacting region at higher flow rates.

Given the successful cooling of the atomizer, future burner designs could consider positioning the atomizer closer to the reaction zone if needed in order to minimize recirculation zones created near the atomizing horn. Ultimately, the potential of this atomizer for combustion applications was demonstrated.

4. Conclusions and outlook

In this study, the HyMAm-Flex (v18) [29], a novel, multi-fuel research burner was characterized at 18 distinct operating conditions, showing stable flames, and some unstable flames, for single-, dual-, and ternary-fuel operating conditions. The HyMAm-Flex burner geometry integrates an ultrasonic atomizer for generating the alcohol spray. This study further demonstrated the successful integration of an ultrasonic atomizer in a high-temperature combustion environment, provided effective cooling measures were applied. This burner is unique in that it is both fuel flexible and enables the investigation of interactions between gaseous carbon-free fuels and liquid carbon-neutral fuels. The study provided an initial experimental characterization of the burner concept and demonstrated broad fuel flexibility, sustaining stable flames for H_2, C_2H_5OH, and their binary and ternary mixtures with NH_3 under stoichiometric conditions.

Chemiluminescence imaging was used to qualitatively discuss flame structure and provide insight into the reaction zones. For selected ternary-fuel operating conditions, exhaust gas measurements were employed to quantify nitrogen-containing pollutants. In the present study, the addition of NH_3 was associated with a reduction in the chemiluminescence intensity of the central flame and increased NH_3 slip and N_2O emissions. The subsequent addition of ethanol appeared to enhance flame stability and was accompanied by reductions in nitrogen-containing emissions over the range of conditions investigated, although these benefits did not continue to increase with further ethanol addition. The present study was limited to the operating conditions investigated, and isolating the effects of fuel composition and flow conditions was not considered. This study, however, highlighted the complex interplay between fuel composition and pollutant formation and points to the need for further systematic studies.

Under the ternary-fuel operating conditions, a stable flame was maintained up to energy fractions of 27% H_2, 38% NH_3, and 35% C_2H_5OH. This study suggests that blending carbon-neutral fuels with carbon-free fuels may enhance flame stability while reducing greenhouse gas and NO_x emissions under the conditions investigated. Limitations to the fuel flexibility are discussed in length, providing potential improvements to burner geometry to improve the overall fuel flexibility. These proposed improvements include enhancing turbulent mixing within the central flame and improving the internal flow of gases through the burner while maintaining the same combustion strategy. Further recommendations are provided in order to more fully characterize the burner performance. Beyond this study, future work is planned using the same burner architecture to address the limitations in fuel flexibility discussed here. Future studies are planned using a more developed version of the HyMAm-Flex incorporating the proposed geometric improvements. These studies will provide a more detailed characterization of the complex interactions between fuels and investigate additional approaches for enhancing flame stability and reducing nitrogen-containing pollutants, further supporting the development of fuel-flexible strategies for low-emission, carbon-neutral energy systems.

CRediT authorship contribution statement

Kristen Morse: Writing – original draft, Visualization, Methodology, Investigation, Formal analysis. **Nele Kretzer:** Writing – review & editing, Resources, Methodology, Investigation. **Chandra P. Singh:** Writing – review & editing, Methodology, Investigation. **Jiawei Wan:** Writing – review & editing, Validation, Methodology, Investigation. **Daniel Kretzler:** Writing – review & editing, Resources, Methodology, Investigation. **Tobias Grimm:** Writing – review & editing, Supervision, Conceptualization. **Björn Stelzner:** Writing – review & editing, Supervision, Conceptualization. **Dimosthenis Trimis:** Writing – review & editing, Supervision, Project administration, Funding acquisition. **Eva Gutheil:** Writing – review & editing, Supervision, Project administration, Funding acquisition. **Jan T. Sehrt:** Writing – review & editing, Supervision, Project administration, Funding acquisition. **Günter Brenn:** Writing – review & editing, Supervision, Project administration, Funding acquisition.

Declaration of competing interest

The authors declare that they have no known competing financial interests or personal relationships that could have appeared to influence the work reported in this paper.

The author is an Editorial Board Member/Editor-in-Chief/Associate Editor/Guest Editor for this journal and was not involved in the editorial review or the decision to publish this article.

Acknowledgments

This work is funded by the German Research Foundation (DFG) through SPP 2419, project numbers 523837500 and 523876164.

Data availability

Data will be made available on request.

References

[1] United Nations Framework Convention on Climate Change. Paris agreement. 2015, Adopted at the 21st Conference of the Parties (COP21), Paris.
[2] Lieuwen T, Emerson B, Acharya V, Gupta I. Roles for combustion in a net-zero CO_2 society. Proc Combust Inst 2024;40.
[3] Sterner M, Stadler I. Handbook of energy storage: Demand, technologies, integration. Springer; 2019.
[4] Griffiths JF. Flame and combustion. Routledge; 2019.
[5] Kohse-Höinghaus K, Oßwald P, Cool TA, Kasper T, Hansen N, Qi F, Westbrook CK, Westmoreland PR. Biofuel combustion chemistry: from ethanol to biodiesel. Angew Chem Int Ed 2010;49:3572–97.
[6] Kim H, Byun M, Lee B, Lim H. Carbon-neutral methanol synthesis as carbon dioxide utilization at different scales: Economic and environmental perspectives. Energy Convers Manage 2022;252:115119.
[7] Pitsch H. The transition to sustainable combustion: Hydrogen- and carbon-based future fuels and methods for dealing with their challenges. Proc Combust Inst 2024;40:105638.
[8] Glassman I, Yetter RA, Glumac NG. Combustion. Academic Press; 2014.
[9] Funke H-W, Beckmann N, Keinz J, Horikawa A. 30 years of dry-low-NOx micromix combustor research for hydrogen-rich fuels—An overview of past and present activities. J Eng Gas Turbines Power 2021;143:071002.
[10] Djinović P, Schüth F. Chapter 12 - energy carriers made from hydrogen. In: Moseley PT, Garche J, editors. Electrochemical energy storage for renewable sources and grid balancing. Elsevier; 2015, p. 183–99.
[11] Agustin V-M, Syed M, Daniel P, Phil B. Ammonia. Renew Fuels 2022;245–74.
[12] Kretzler D, Puri R, Stelzner B, Zirwes T, Hagen FP, Stein OT, Trimis D. Experimental and numerical investigation of non-premixed ammonia flames stabilized on a heated slot burner. Proc Combust Inst 2025;41:105854.
[13] Howarth T, Day MS, Pitsch H, Aspden A. Thermal diffusion, exhaust gas recirculation and blending effects on lean premixed hydrogen flames. Proc Combust Inst 2024;40:105429.
[14] Valera-Medina A, Morris S, Runyon J, Pugh DG, Marsh R, Beasley P, Hughes T. Ammonia, methane and hydrogen for gas turbines. Energy Procedia 2015;75:118–23.
[15] Valera-Medina A, Marsh R, Runyon J, Pugh D, Beasley P, Hughes T, Bowen P. Ammonia–methane combustion in tangential swirl burners for gas turbine power generation. Appl Energy 2017;185:1362–71.
[16] Valera-Medina A, Pugh D, Marsh P, Bulat G, Bowen P. Preliminary study on lean premixed combustion of ammonia-hydrogen for swirling gas turbine combustors. Int J Hydrog Energy 2017;42:24495–503.
[17] Mashruk S, Vigueras-Zuniga MO, Tejeda-del Cueto M-E, Xiao H, Yu C, Maas U, Valera-Medina A. Combustion features of CH4/NH3/H2 ternary blends. Int J Hydrog Energy 2022;47:30315–27.
[18] Marshall A, Venkateswaran P, Noble D, Seitzman J, Lieuwen T. Development and characterization of a variable turbulence generation system. Exp Fluids 2011;51:611–20.
[19] Rajagopalan HP, Emerson B, Acharya V, Noble D, Lieuwen T. Measurements of CO and NOx emissions from premixed turbulent methane/hydrogen flames. J Eng Gas Turbines Power 2026;148:041004.
[20] Meng X, Liu L, Qin M, Miao M, Zhao H, Long W, Bi M. Study on ammonia/methanol blends with ammonia cracking for low-carbon combustion and NO reduction. J Clean Prod 2024;450:141959.
[21] Elbaz AM, Albalawi AM, Wang S, Roberts WL. Stability and characteristics of NH3/CH4/air flames in a combustor fired by a double swirl stabilized burner. Proc Combust Inst 2023;39:4205–13.
[22] Xu L, Elbaz AM, Cenker E, Sim J, Bai X-S, Roberts WL. Reduction of NOx emissions in ammonia combustion using a double-flame premixed co-combustion concept. Proc Combust Inst 2024;40:105748.
[23] Sobhani S, Muhunthan P, Boigné E, Mohaddes D, Ihme M. Experimental feasibility of tailored porous media burners enabled via additive manufacturing. Proc Combust Inst 2021;38:6713–22.
[24] Runyon J, Giles A, Marsh R, Pugh D, Goktepe B, Bowen P, Morris S. Characterization of additive layer manufacturing swirl burner surface roughness and its effects on flame stability using high-speed diagnostics. J Eng Gas Turbines Power 2020;142:041017.
[25] Lacas F, Versaevel P, Scouflaire P, Coeur-Joly G. Design and performance of an ultrasonic atomization system for experimental combustion applications. Part Part Syst Charact 1994;11:166–71.
[26] Namiyama K, Nakamura H, Kokubo K, Hosogai D. Development of ultrasonic atomizer and its application to SI engines. SAE Trans 1989;701–11.
[27] Peskin RL, Raco RJ. Ultrasonic atomization of liquids. J Acoust Soc Am 1963;35:1378–81.
[28] Turns SR. In: Introduction to combustion, vol. 287, McGraw-Hill Companies; 1996.
[29] Kretzer N, Morse K, Wan J, Singh CP, Gutheil E, Brenn G, Grimm T, Sehrt JT. Development of a fuel-flexible research burner for hydrogen, ammonia, and methanol combustion using additive manufacturing. Nano Micro Mech Rev 2026.
[30] DIN ISO/ASTM 52900:2022-03 : Additive manufacturing — General principles — Terminology. 2021, German edition.
[31] Frazier WE. Metal additive manufacturing: a review. J Mater Eng Perform 2014;23:1917–28.
[32] DebRoy T, Wei HL, Zuback JS, Mukherjee T, Elmer JW, Milewski JO, Beese AM, Wilson-Heid Ad, De A, Zhang W. Additive manufacturing of metallic components–process, structure and properties. Prog Mater Sci 2018;92:112–224.
[33] Santecchia E, Spigarelli S, Cabibbo M. Material reuse in laser powder bed fusion: Side effects of the laser—metal powder interaction. Metals 2020;10:341.
[34] Chowdhury S, Yadaiah N, Prakash C, Ramakrishna S, Dixit S, Gupta LR, Buddhi D. Laser powder bed fusion: a state-of-the-art review of the technology, materials, properties & defects, and numerical modelling. J Mater Res Technol 2022;20:2109–72.
[35] Hosseini E, Popovich VA. A review of mechanical properties of additively manufactured inconel 718. Addit Manuf 2019;30:100877.
[36] Baukal C, Eleazer P. Quantifying NOx for industrial combustion processes. J Air Waste Manage Assoc 1998;48:52–8.
[37] Gaydon A. The spectroscopy of flames. Springer Science; 2012.
[38] Konnov AA. An exploratory modelling study of chemiluminescence in ammonia-fuelled flames. Part 2. Combust Flame 2023;253:112789.
[39] Zhu X, Roberts WL, Guiberti TF. UV-visible chemiluminescence signature of laminar ammonia-hydrogen-air flames. Proc Combust Inst 2023;39:4227–35.
[40] Zhu X, Khateeb AA, Roberts WL, Guiberti TF. Chemiluminescence signature of premixed ammonia-methane-air flames. Combust Flame 2021;231:111508.
[41] Karan A, Dayma G, Chauveau C, Halter F. Insight into the inner structure of stretched premixed ammonia-air flames. Proc Combust Inst 2023;39:1743–52.
[42] The MathWorks, Inc. MATLAB. Natick, Massachusetts, United States: The MathWorks, Inc.; 2026, Version R2026a.
[43] Wang D, Tian Z-Y, Li Q-L, Kuang J-J, Yu X-P. Kinetic analysis on the hydrogen cyanide formation in the premixed methane/ammonia flame. Fuel 2025;380:133046.
[44] Morse K, Berglez P, Brenn G. Experiments and linear stability analysis of spray formation by an ultrasonic atomizer. In: ILASS europe 2025. Lund, Sweden; 2025, Available: https://rb.gy/d8pkuw.
[45] Glarborg P, Miller JA, Ruscic B, Klippenstein SJ. Modeling nitrogen chemistry in combustion. Prog Energy Combust Sci 2018;67:31–68.
[46] Kobayashi H, Hayakawa A, Somarathne KKA, Okafor EC. Science and technology of ammonia combustion. Proc Combust Inst 2019;37:109–33.